Understanding mechanical stresses upon solid-state battery electrode cycling using discrete element method

Mohammed Alabdali [a,b], Franco M. Zanotto [a,b], Mehdi Chouchane [c], Alain C. Ngandjong [a,b], Virginie Viallet [a,b], Vincent Seznec [a,b,d], Ying Shirley Meng [c,e], Alejandro A. Franco [a,b,d,f,*]

[a] *Laboratoire de Réactivité et Chimie des Solides (LRCS), Université de Picardie Jules Verne, Hub de l'Energie, UMR CNRS 7314, 15 rue Baudelocque, 80039 Amiens, France*
[b] *Réseau sur le Stockage Electrochimique de l'Energie (RS2E), Hub de l'Energie, FR CNRS 3459, 15 rue Baudelocque, 80039 Amiens, France*
[c] *Pritzker School of Molecular Engineering, University of Chicago, Chicago, IL 60637, USA*
[d] *ALISTORE-European Research Institute, Hub de l'Energie, FR CNRS 3104, 15 rue Baudelocque, 80039 Amiens, France*
[e] *Department of NanoEngineering, University of California San Diego, La Jolla, CA 92093, USA*
[f] *Institut Universitaire de France, 103 boulevard Saint Michel, Paris 75005, France*

ARTICLE INFO

ABSTRACT

Solid-state batteries (SSBs) often fall behind conventional lithium-ion batteries (LIBs) in performance. Electrochemical cycling protocols, in particular under isostatic compression, present ample opportunities for improvement to mitigate issues like contact loss and aging among numerous other challenges. This study introduces a novel Discrete Element Method (DEM) workflow to assess the effectiveness of uniaxial and isostatic compression as proceeding electrode preparation on the conductivity and structural integrity of SSBs. Isostatic compression achieves conductivity levels comparable to uniaxial compression with significantly reduced pressure requirements. In contrast, uniaxial compression at elevated loads, while resulting in higher conductivity, subjects the particles to significant stress, increasing the risk of cracking and deformation of the SSB materials. This study shows the impact of mechanical stress during different stages of electrochemical cycling on the microstructure's integrity to provide valuable insights into electrochemistry-mechanics couplings, which can be challenging to evaluate experimentally.

1. Introduction

The advent of Lithium-ion batteries (LIBs) has been pivotal in revolutionizing modern society, transforming electrochemical energy storage and playing a crucial role in electric automotive applications [1]. However, the escalating global decarbonization push necessitates a next-generation battery surpassing the energy densities and power performances of current LIBs to diminish reliance on fossil fuels [2].

In response to this imperative, solid-state batteries (SSBs) have emerged as promising alternatives due to their potential for heightened energy density and improved safety features [3]. Yet, their performance lags behind conventional LIBs, largely due to the intricate structural and electro-chemical transformations within the SSB environment [4,5], These mechanisms, absent in liquid electrolyte systems, underscore the critical need to comprehend the dynamics at solid/solid interfaces for advancing SSBs [6–11], such as chemo-mechanical reactions and active

material (AM) cracking, along with other phenomena taking place at the microscopic scale. Many of these phenomena are coupled with the intricate interplay between electrochemical processes and material mechanics lying at the heart of SSB enhancement [11–13]. Stress evolution and void occurrence at the interface particularly underscore the chemo-mechanical effects that are expected to be more pronounced in SSBs due to their configuration [6,11–13].

The manufacturing process significantly influences the chemo-mechanical compatibility, dictating the battery cell's final performance. A study by Shi et al. [14], engaging experiments with Discrete Element Method (DEM) modeling, highlights the role of cathode particle size ratios in influencing SSB capacity, elucidating the impact of particle size distribution (PSD) on electrochemical performance. They defined "cathode utilization" as the ratio of the volume of accessible AM particles in contact with solid electrolyte (SE) network, to the total volume of AM particles (V_{AM}^{active}/V_{AM}) and assessed it in comparison to "λ", where λ

is a function of the ratio of the particle size of cathode AM to the particle size of the SE ($\lambda = D_{AM}/D_{SE}$). Therefore, large AM particle sizes, in their case, can significantly enhance the capacity of the SSB, since a higher AM loading is enabled by the high ratio of the AM to SE particle size. This prior study has illustrated the role of the PSD of discrete materials on the electrochemical performance, but there are still a number of pressing questions to be answered. In particular, the interplay between stress distribution and structural changes within SSBs during cycling. The impact of the compaction on the final microstructure within SSB composite cathodes has been experimentally shown in literature [15, 16]. This, in turn, affects the internal resistance, the frequency of undesirable (electro)chemical reactions and capacity fading [4]. The latter, primarily induced by contact loss due to volume changes during cycling, remains a critical hurdle [6,17]. Addressing these challenges necessitates a focus on materials pretreatment, solid/solid interfaces, and processing techniques [8].

Mitigating aging in SSBs has been explored through various cycling protocols, with isostatic compression emerging as a promising method. This approach, involving the uniform application of pressure during cycling, shows the potential to improve capacity retention and cycle life by enhancing electrode microstructure uniformity [10,18–20]. Further insight into aging mechanisms, particularly the cracking of AM, can be gleaned from 3D modeling. These models offer a deeper understanding of composite electrode microstructures, aiding in predicting interface evolution and void formation, essential for more efficient and durable SSBs [11,21].

The lack of comprehensive 3D models that address material interfaces and mechanics remains a gap in current research. While some studies [11] focus on specific SSB systems (*e.g.* Polymer SSBs, sulfides, and garnets), the need for dynamic 3D-resolved models to capture the interfacial evolution between materials upon electrochemical cycling within composite cathodes remains unmet. In the ARTISTIC initiative, we have produced pioneering 3D-resolved physics-based models to predict how manufacturing parameters impact LIB electrode microstructures [22–25]. We have also demonstrated the transferability of this approach by simulating the wet processing of SSB cathodes [26,27]. In this research, we aim to address the gap in understanding the effects of stress distribution during (de)lithiation, which is often overlooked in different experimental compression approaches for SSBs. This is achieved by simulating the manufacturing of composite electrodes under realistic conditions, involving high uniaxial pressure followed by low isostatic pressure. Our approach involves developing a 3D-resolved computational model to assess mechanical stress distribution during compaction and cycling under isostatic compression. The state-of-the-art computational power limits a full coupling of electro-mechanical numerical simulations with the resulting mechanical behavior within the microstructureon large scales. To the best of our knowledge, this is the first time a model that couples the compression approach with the particle mechanical changes during electrochemical cycling is proposed.

2. Methods

2.1. Simulation workflow

We present in this article a computational workflow that allows simulating the manufacturing (following the protocol in reference [28]) by compressing SSB composite cathodes and characterizing their electrochemical behavior during uniaxial compression and cycling under isostatic compression. The simulated composite cathodes consist of two types of materials LiNi$_{0.5}$Mn$_{0.3}$Co$_{0.2}$O$_2$ (NMC532) as AM and Li$_6$PS$_5$Cl (LPSCl) as SE with a composition of 73.30 wt.% and 26.7 wt.%, respectively, and a PSD varying from 3–10 μm and 6–13 μm, respectively, shown in Fig. S1 in the Supplementary Information (SI). AM and SE particles' location are stochastically generated in an initial volume, and then uniaxially compressed at 375 MPa to ensure a high level of

structural compactness. The load on the microstructure is then relaxed to 1 atm to simulate the process of transferring to an isostatic compressor. Finally, the AM particles are sequentially expanded and contracted in order to mimic electrochemical cycling conditions under 1 - 5 MPa of isostatic pressure applied in the three dimensions.

All simulations are carried out using LIGGGHTS software [29] on one node of MatriCS platform (Université de Picardie Jules Verne) with 375 GB of RAM and 1 processor (Intel® Xeon® Gold 6148 CPU @ 2.40 GHz, 40 cores). The objective of each simulation step is to output a 3D microstructure of the electrode by solving the Newtonian equations of motion. At each step, the boundary conditions are kept fixed for dimensions perpendicular to the pressing planes. At the uniaxial compression, the boundary conditions are periodic for x and y lateral dimensions and fixed for the z dimension. Then, the boundary conditions are kept without changes until the step of isostatic compression in the workflow (Fig. 1), which requires all boundary conditions to be fixed. The output microstructure of each step is used as an input for the next step in order for the workflow to proceed. Young Modulus, Poisson ratio, Friction coefficient and Restitution coefficient values of the AM and SE were retrieved from references [30,31] and used as Granular Force Field (GFF) parameters. More information about the GFF can be found in the SI.

2.1.1. Initial microstructure generation

To initialize the simulation workflow, a microstructure with 11,002 particles of two types (AM and SE) and 14.96 mg/cm^2 AM mass loading is generated by placing particles in randomly selected locations within a simulation box of $150 \times 150 \times 150$ μm^3. The simulations run in the NVE ensemble with an initial temperature of 300 K, meaning that the number of particles, simulation box volume and energy are conserved throughout the simulation workflow. This workflow is repeated with different initial particle arrangements achieved by changing the random seeds of particle localization to obtain 2 microstructures (M1 and M2) at each step for comparison.

2.1.2. Uniaxial compressing

The generated initial microstructure is then used as an input for the simulation of the uniaxial compression, where the boundary conditions of the x and y dimensions remain periodic, but the z dimension is fixed. However, we imitate the uniaxial compression by applying forces on the modeled microstructure along the z axis, as shown in Fig. 2 and in a supplemental video. This involves two moving planes to compress the microstructure with a force gradually increasing relative to the resistance exerted by the microstructure until it reaches a maximum pressure of 375 MPa over an area of 150×150 μm^2. The simulation runs until most values remain constant, *i.e.*, the position of the plane on which the force is imposed, the force exerted on the plane, and the positions of the particles. Typically, this involves 400 μs of simulation time as we have already done tests with longer simulation time without noticing a significant difference. The pressure applied by the planes is then gradually reduced back to ambient pressure in the same way.

2.1.3. Isostatic compressing

The uniaxially compressed microstructure is used in this simulation step as an input, shown in Fig. 3 and in a supplemental video. At this stage, all the boundary conditions are fixed at the dimensions of the simulation box. During the isostatic pressing, the microstructure was subjected to three different pressure values (1, 3 and 5 MPa) applied to the surface area of each side of the electrode to approximate isostatic compression. This range was chosen based on the experimental protocol in reference [28] with 5 MPa being the upper operational range of the device. Then, the size of all AM particles was expanded and contracted by 6 % [32,33] for five consecutive cycles to model their behavior upon lithiation and delithiation, respectively, occurring during the battery cell electrochemical cycling. In real systems, the size change of AM particles does not occur uniformly because of the heterogeneity in the
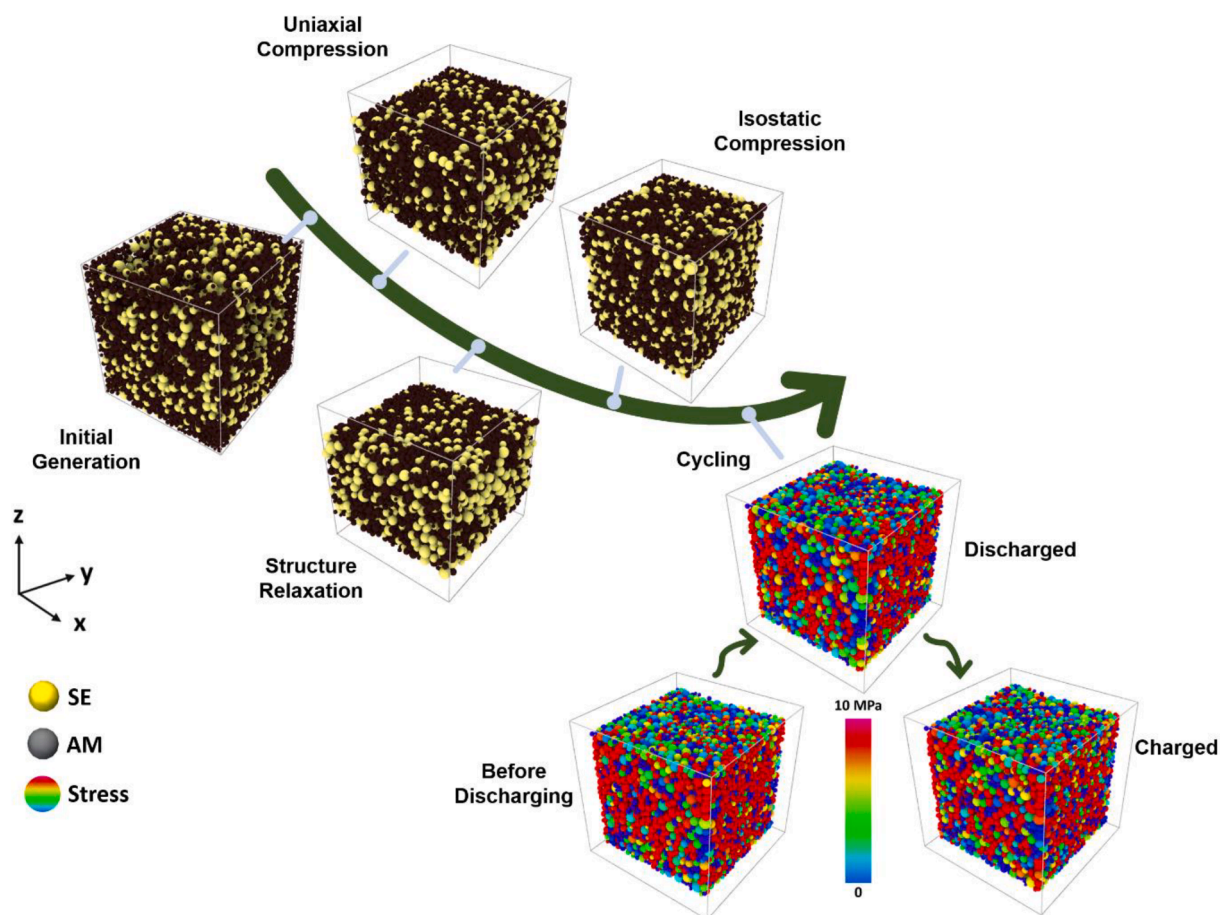
Fig. 1. Schematic representation of the simulation workflow based on the experimental procedure of cycling SSB composite cathodes under isostatic compressing.
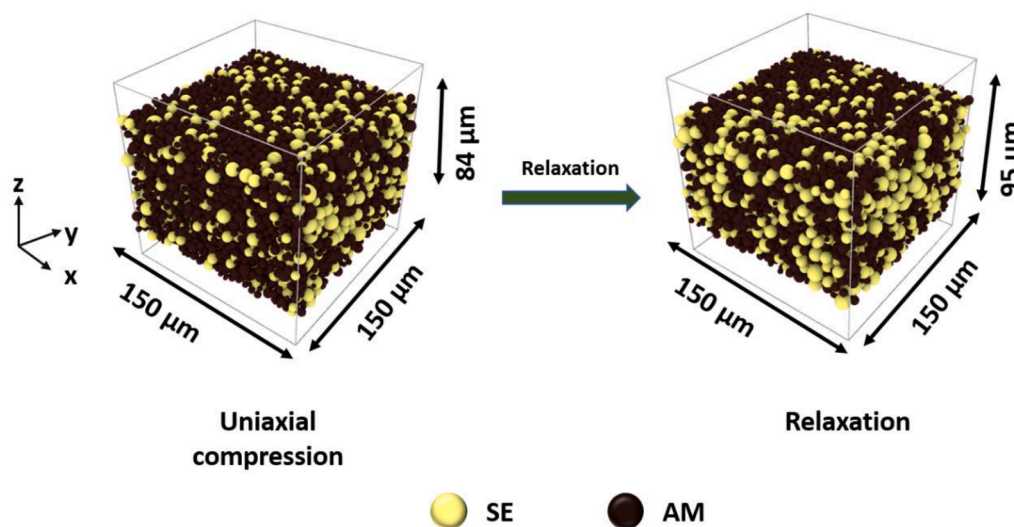

Fig. 2. Representation of the transition of M1 from the uniaxially compressed state to the relaxed state.

interfaces and AM active surface that lead to heterogeneous (de)lith-iation electrochemical kinetics. As a result, when performing numerical electrochemical simulations using microstructures derived from our simulations, symmetrical charge and discharge profiles are anticipated, without difference in potential values since the AM particles revert to their original size after each step. This would be because of the homogeneous AM size change during the DEM simulations. However, by using

this approach, we assume that the DEM model should be able to capture the effects of isostatic compression on the microstructure allowing for a comprehensive analysis of the resulting microstructural changes and stress distribution within the electrode during electrochemical cycling under applied pressure. Furthermore, our group is currently focused on developing numerical simulations that couple the electrochemical response with the mechanical behavior during (de)lithiation, which is a
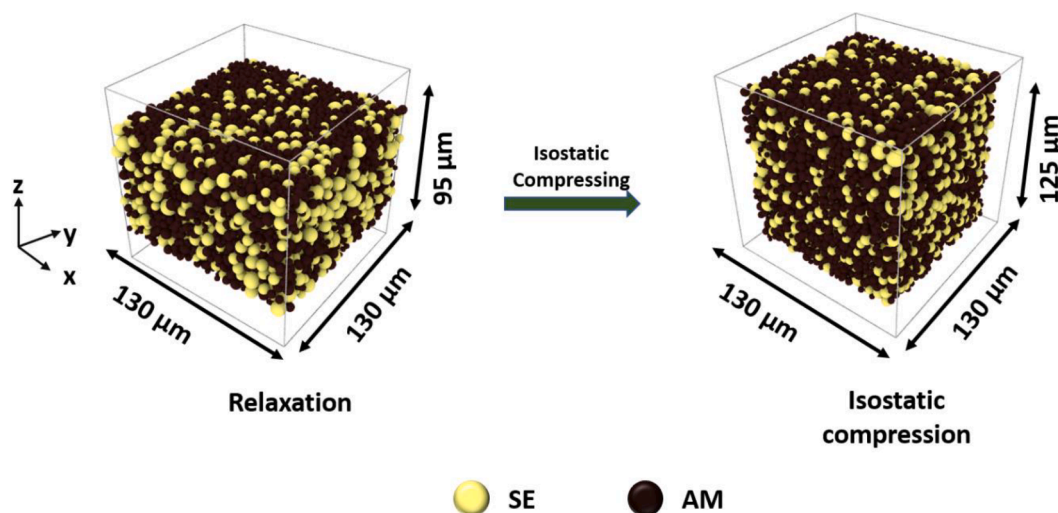
Fig. 3. Representation of the transition of M1 from the relaxed state to the isostatically compressed state.

challenging task beyond the scope of this publication.

2.1.4. Electronic conductivity and ionic geometrical tortuosity factor calculations

In order to analyze the microstructural characteristics of the electrode, we use physical properties and geometrical descriptors. We used the effective electronic conductivity σ_{el} arising from the percolated network of AM particles, and the geometrical tortuosity τ for ionic conduction along the percolated network of SE particles. The σ_{el} and τ of the microstructures serve as quantitative indicators for the impact of the compressing protocol on the electrode's electrochemical performance. These parameters provide a simple means of assessing both the ionic and electronic properties of the simulated electrodes.

To determine σ_{el} of the AM network and τ of the SE network within the microstructures, electronic and ionic current fluxes simulations were performed using ConductoDict and DiffuDict modules in GeoDict [34] software. The simulations of the current fluxes through the composite electrode involves reconstructing the microstructures by discretizing them into voxels, which are generated based on the output microstructures from DEM simulations. For this, a simple Python script was used, selecting a voxel length of 0.5 μm. Given the nature of the DEM simulations, particles present some overlap. The voxels corresponding to a region of the overlap between SE and AM are assigned to AM due to its higher Young's modulus. The current fluxes simulations are conducted with a potential difference of 1 V along the thickness of the electrode. The results of the simulations are then normalized by the bulk conductivity value of AM.

To calculate σ_{el}, the Poisson equation is solved within the simulation domain by applying a 1 V potential difference between opposite sides along the z direction. Ohm's law is then utilized to obtain σ_{el}. Periodic boundary conditions are considered for the outer lateral planes of the microstructures. In the simulation, it is assumed that the ionic current is carried by the SE, while the electronic current is carried solely by the AM.

The τ values correspond to the SE, where Li$^+$ ions are transported through. They are determined using the equation $\tau = \sqrt{\eta/D_{eff}}$, where η represents the volume fraction occupied by the SE and D_{eff} is the effective diffusion coefficient for Li$^+$ within the SE conductive media. The calculation of D_{eff} involves solving Fick's first law within the SE domain, considering a concentration difference Δc between the outer xy planes. D_{eff} is obtained from the overall diffusive flux (j) using the equation: $D_{eff} = -j \times length /\Delta c$. Importantly, τ is a geometric property and remains independent of the specific values chosen for Δc and the diffusion coefficient within the SE. Periodic boundary conditions are

applied in lateral dimensions.

3. Results and discussion

There is a strong correlation between the strain and the ionic conductivity of solid materials as suggested in the literature [35], yet the optimization of the cycling protocols through the analysis of stress distribution remains largely unexplored in highly conductive SEs, *e.g.* sulfides, that are pivotal for SSBs. Particularly, the optimization of internal stress is shown to fine-tune the material's mechanical properties [36], and to modulate its thermal and electronic transport [37]. In this section, we assess the effects of uniaxial and isostatic compression on the stress distribution, as well as the ionic tortuosity and electronic conductivity of the SSB cathode. We intend to simulate the fabrication of the composite electrode in real conditions to have an understanding on the stress impact at each step, since the electrode is usually pressed uniaxially at 300–500 MPa before cycling to ensure high compaction [28].

3.1. Uniaxial and isostatic stress distribution

Uniaxial compression necessitates the application of high pressures to achieve optimal microstructural compactness, on top of the disadvantage of increasing the tendency of AM cracking and subsequently shortening the SSB cell lifespan. As illustrated in Fig. 4, the microstructure subjected to uniaxial compression at 375 MPa exhibits a size-dependent stress among the AM particles, particularly noticeable in lateral directions. M2 exhibits the same phenomenon as shown in Fig. S2 and S5 in the SI. Despite the compression being applied solely along the z-axis, smaller AM particles endure stress exceeding 500 MPa in all dimensions. However, stress levels vary depending on the particle type, with AM particles experiencing over twice the stress compared to SE particles across the microstructure thickness. However, particles in the bottom and the top parts of the simulation box experience less stress. The stress in those regions is close to the pressure boundary condition (375 MPa), but the bulk experiences higher stress because it is under the pressure of both top and bottom planes. Another remark is that the stress exerted on the SE particles is reduced by a factor of two with respect of that exerted on the AM, on average, due to the deformability and the lower mechanical stiffness of the SE particles and the overall stress distribution is uniform along all axes.

Conversely, isostatic compression offers a less disruptive alternative, requiring lower pressure levels to maintain comparable microstructural compactness and ensure a more uniform pressure application from all directions. Therefore, the establishment of a meticulously controlled
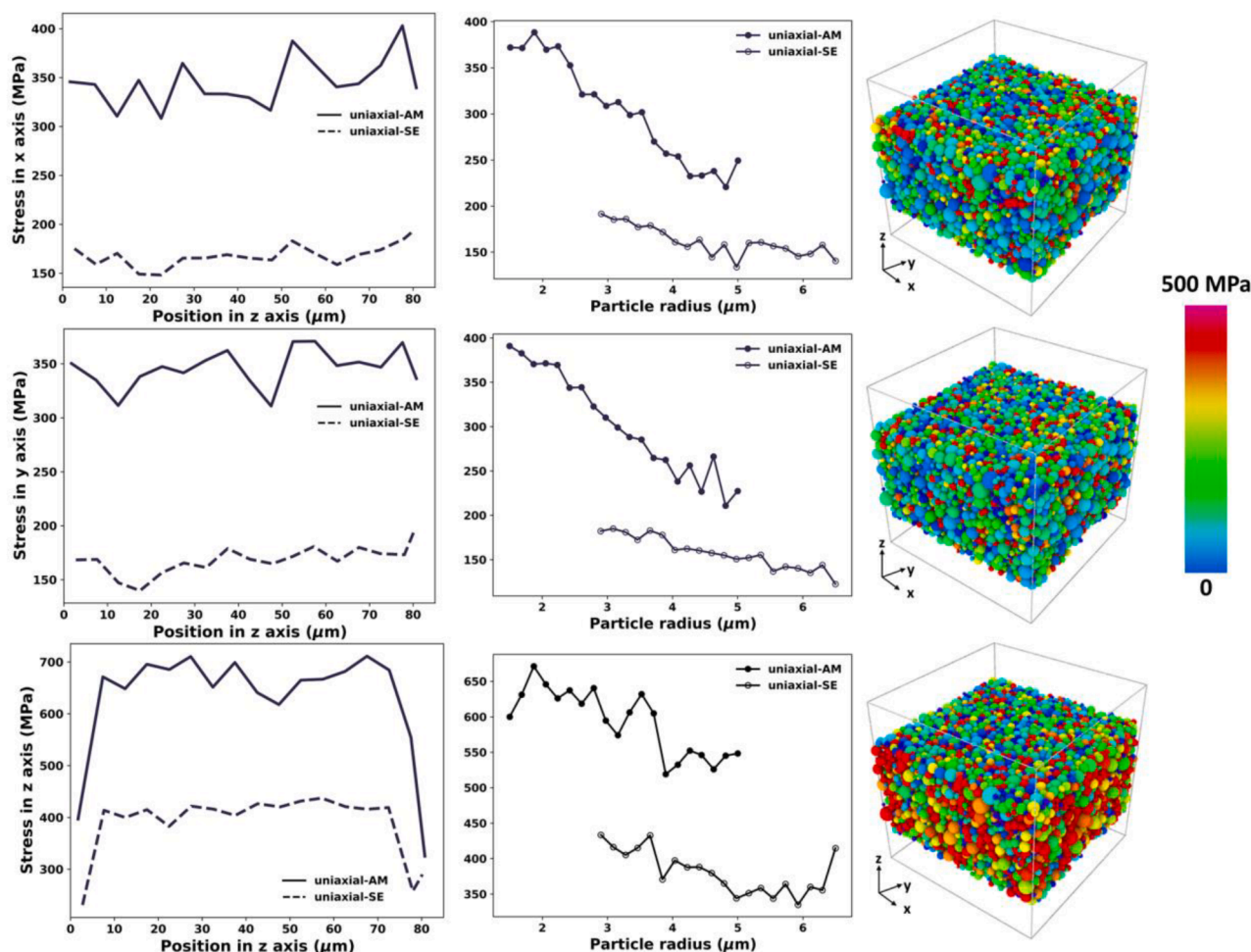
Fig. 4. Average stress exerted on each dimension of M1 as a function of particles' position in z dimension and the radius under 375 MPa uniaxial compression. The microstructure is presented with particles color coded according to the exerted stress on each dimension.

stress distribution becomes imperative for enhancing electrochemical cycling protocols, thereby optimizing the battery cell's overall cycle life and preserving the health of the AM and SE structural integrity. This milder approach not only mitigates the risk of structural damage but also contributes to the sustained performance and longevity of the SSB cell.

Fig. 5a depicts M1 following isostatic compression simulations at 5 MPa, with the maximum applied stress nearly two orders of magnitude lower than uniaxial compression, while still maintaining a well-compacted microstructure. Fig. S6a and b depict the isostatic compression of M1 at 1 and 3 MPa, respectively, while the same information for M2 are shown in Fig. S4 and S7. For uniaxial compression, we observe average stress values of almost 400 MPa along x axis, 380 MPa along y axis and 700 MPa along z axis, while for isostatic compression, stress varies between 6 – 16 MPa along the x and y axes, and 6 – 16 MPa along the z axis. Notably, particles in direct contact with the planes endure higher stress, particularly on larger particles at the edges, gradually decreasing towards the core of the microstructure.

During the discharging phase, AM particles homogeneously expand by 6% in diameter [32,33]. Fig. 5a also highlights increased stress on AM particles as their size grows, corresponding to heightened contact points and forces exerted on them. The lateral stress is slightly higher towards the edges in the x and y dimensions, which decreases towards the core, impacting conductivity due to interruptions along the ionic and electronic pathways. However, a significant shift in stress occurs during the charging phase when AM particles contract back to their original size, leading to a transfer of stress to SE particles as AM particles occupy less volume. This results in a more homogeneous stress distribution across the microstructure thickness after the charge.

Before the AM size increases to simulate discharging, AM experiences higher stress compared to SE particles due to the deformable and soft nature of the SE. This gap in stress levels widens with AM particle expansion under load in a strictly compact volume creating more stress points. Eventually, the stress gap decreases until both AM and SE particles are exposed to similar stress levels (Fig. 5a and b) as AM contracts back to its original size. Furthermore, the analysis of the average exerted stress as a function of particle radius reveals a clear correlation between particle size and stress, with smaller AM particles experiencing higher stress compared to larger ones. This underscores the importance of considering particle properties and pretreatments while manufacturing SSB electrodes, as they determine stress distribution magnitude on the microstructure.

From Fig. 5b (as well as S8a, S8b, and S8c in the SI), it is evident that the average stress applied across the cross-sectional area (xy plane) of the microstructure exhibits considerable heterogeneity. This variation arises from differences in the distribution of AM within the microstructure, despite both configurations having identical mass loadings. M2 notably displays a higher degree of stress variation compared to M1, particularly in the lower half of the y dimension. This concentrated stress distribution generates more prominent ionic percolation pathways, thereby enhancing the overall structural Li$^+$ diffusivity. In reference [38] from our group, Torayev et al. used tomography imaging to reconstruct lithium−oxygen cathode microstructures to simulate the electrochemical performance based on the impact of pores arrangement and interconnectivity. They pointed out that exact pore locations can
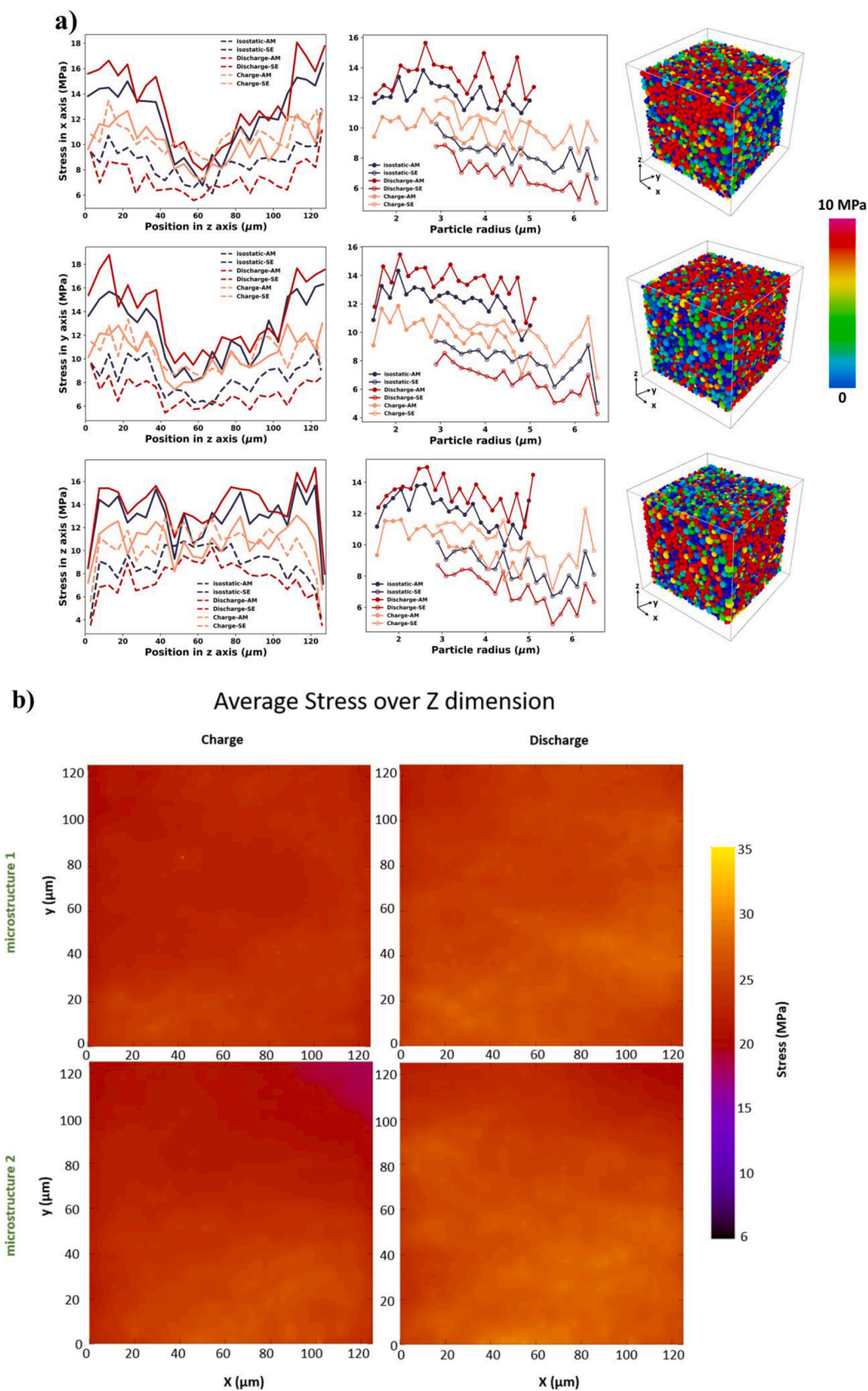
Fig. 5. a) Average stress exerted on each dimension of M1 as a function of particles' position in z dimension and the radius under 5 MPa isostatic compression. The microstructure is presented with particles color coded according to the exerted stress on each dimension. b) Heatmaps of exerted stress in z dimension at the discharged and charged states over the xy cross-section of M1 and M2 under 5 MPa isostatic compression.

imply different performances, despite of two electrodes having the same overall porosity. Therefore, local geometrical heterogeneities in the conductive medium (stress induced SE particle arrangement in our case) has significant impact on the electrochemical performance of such systems.

3.2. Electronic conductivity and ionic geometrical tortuosity factor calculations

Isostatic pressing at low pressures demonstrates the potential to achieve conductivity levels comparable to those attained through uniaxial pressing at nearly twice the order of magnitude. This presents a promising avenue for processing SSB cathodes, particularly when considering that uniaxial processes typically demand pressing pressures of up to 500 MPa. Fig. 6a and b show the evolution of σ_{el} and τ, respectively, from the uniaxial pressing step to the charge of the fifth

cycle under isostatic compression. The pressure applied by the isostatic compression ranges from 1 MPa to 5 MPa (Fig. 6) whereas each of the two different microstructures is represented with a different marker shape. The σ_{el} is normalized by the electronic conductivity of the AM (σ_{AM}) to demonstrate the influence of particle arrangement. Similarly, D_{eff} is normalized by the diffusion coefficient for Li$^+$ ions within bulk SE (D_{SE}) in Fig. S9 in the SI. Since the same resulting microstructures (M1 and M2) from the preceding uniaxial compressing and relaxation steps are used as initial step to be compressed by 1, 3 and 5 MPa isostatically, their corresponding data points are superposed because they exhibit the same σ_{el}, τ and D_{eff} values in Fig. 6 and S9.

Uniaxial compression at 375 MPa leads to microstructure compaction, resulting in reduced thickness and increased contact points between particles, thus yielding higher σ_{el} values compared to subsequent steps. However, a significant decrease is observed upon relaxation, followed by partial recovery during isostatic compression. As AM particles
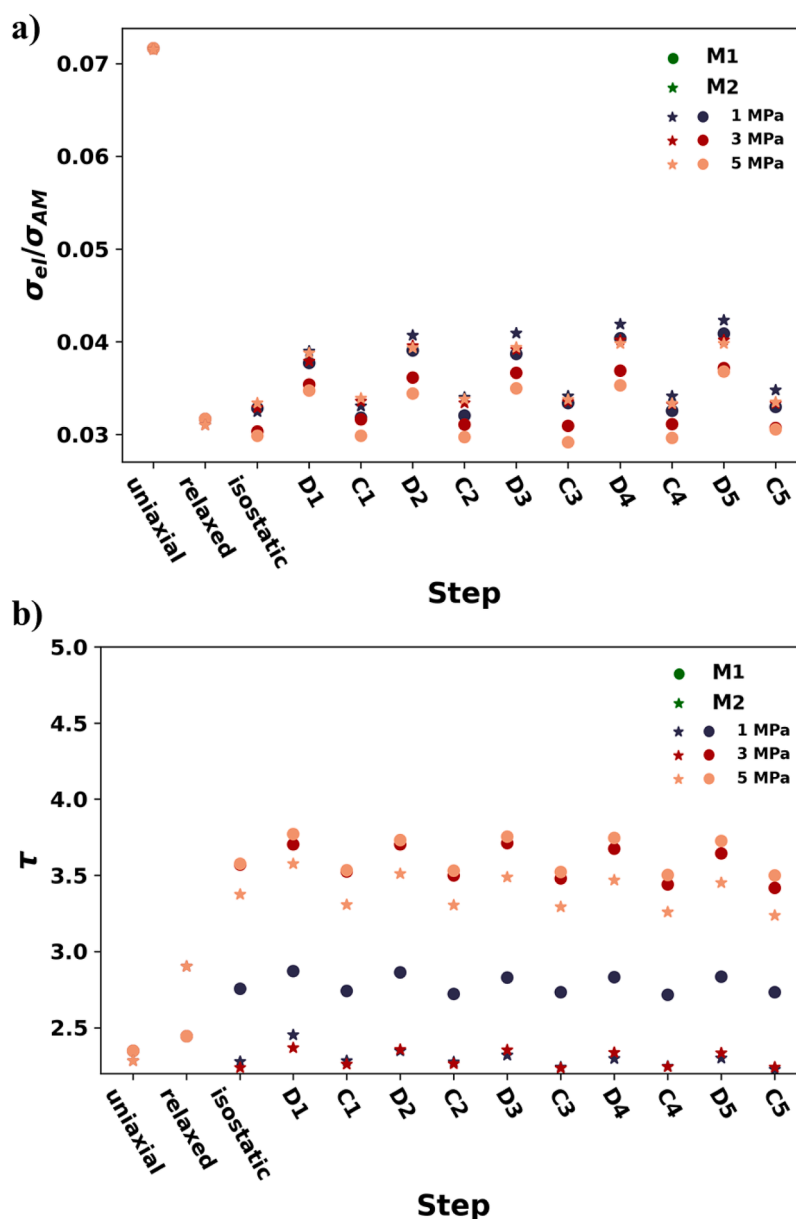

Fig. 6. a) Electrodes' σ_{el} evolution normalized by the conductivity of the AM (σ_{AM}) of the microstructures resulting from different isostatic compressions. b) Electrodes' τ evolution for the microstructures resulting from different isostatic compressions. The x axis represents the microstructures resulting from different steps in the modeling workflow where Di and Ci refer to the discharging and charging for the ith time under isostatic compression. The green markers in the legend are aimed to differentiate the two microstructures and are not used for data representation.

expand, increasing in volume, σ_{el} rises and then declines upon returning to their original size during the isostatic step. Nevertheless, the σ_{el} exhibit a monotonic increase with increasing isostatic pressure. It should be noted that we are not accounting for the change of electronic conductivity of AM in its lithiated and delithiated states, therefore our resulting values can be attributed to changes in geometry only. Despite yielding more compact microstructures with higher σ_{el} values, uniaxial pressing subjects AM and SE particles to stress ranges between 300 – 400 MPa and 150 – 200 MPa, respectively, rendering AM particles susceptible to cracking and SE particles to deformation. Hence, conductive carbon is often added to achieve elevated σ_{el} values and mitigate associated issues [4].

The initial particle arrangement exhibits a noticeable impact on τ and D_{eff} values, as shown in Fig. 6b and S9, albeit within the margin of error. Differences in τ and D_{eff} values stem from distinct ionically conductive pathways resulting from varying SE particle arrangement. Furthermore, τ and D_{eff} values displayed by the microstructures do not exhibit a monotonic dependence on the pressure of isostatic compression. As demonstrated in Fig. 6b and S9, the lowest τ and highest D_{eff} are observed in a structure isostatically compressed at 1 MPa, followed by 3 MPa and 5 MPa. The second microstructure exhibits D_{eff} values close to those of uniaxial pressing and even surpasses it in the case of τ. This may be attributed to lower pressure allowing for easier particle rearrangement; however, further investigation is needed to fully understand this phenomenon.

According to a systematic examination of interlaboratory reproducibility [39], there is a significant challenge in comparing absolute measured ionic conductivity values reported in the literature. After distributing identical samples to multiple research laboratories for characterization, their conductivity determinations present considerable variability. The measured total ionic conductivity exhibited large ranges of up to 4.5 mS cm^{-1} (1.3–5.8 mS cm^{-1} for the most conductive sample, with a relative standard deviation ranging from 35% to 50% across all samples). This variation depends on the stress impact the SE particles arrangement and the interruptions in its conductive network. Thus, it is expected to have such variation in τ and D_{eff} values between the two microstructures simulated (Fig. 6b and S9). Fig. 5b and Supplementary Fig. S8a, b, and c collectively suggest that the augmented diffusivity observed in M2, as opposed to M1, may stem from stress variation. Specifically, regions within the cross-sectional area exhibiting elevated average stress along the z dimension play a role in compacting SE particles influencing the microstructure to have higher the overall diffusivity and tortuosity.

In reference [4], Bielefeld et al. conducted an evaluation of the influence of a cone-like microstructure, characterized by the arrangement of AM and SE particles into conic pillars in direct contact, compared with a microstructure featuring stochastically arranged AM and SE particles. Their results indicate that the cone-like microstructure demonstrated notably enhanced values of active interface area compared to the stochastic counterpart and experimental outcomes. Our findings, in addition to Bielefeld's, show that enhanced structural arrangements contribute to improved values of τ and D_{eff}. However, achieving advancements in overall SSB performance necessitates further development.

Based on these observations, we found that isostatic compression of electrodes involving low-pressure application yields well-compacted electrodes with σ_{el} and τ values comparable to larger applied pressures in uniaxial mode, at less material damage. The observed trend also indicates that σ_{el} values increase with isostatic pressures exceeding 5 MPa (demonstrated in Fig. S10), yet decrease when pressures fall below 1 MPa. Nonetheless, optimal isostatic compression pressures must be further refined to achieve optimal τ and D_{eff} values (the attempt to simply increase the isostatic pressure is not sufficient as shown in Fig. S10b and c), thereby promoting the formation of a less tortuous SE network. It is noteworthy that (pre-)processing conditions, modeled by the difference of microstructural arrangement between M1 and M2,

have a substantial impact on the microstructures, necessitating their optimization to complement the enhancement of the SE network characteristics. This theoretical result is still in agreement with the experimental work published in reference [28]. Nevertheless, incorporating smaller AM particles in SSB composite cathode design is still recommended, in the literature, to enhance mechanical stability and improve electrochemical performance during cycling [40–42].

4. Conclusion

We present a DEM workflow that provides a comprehensive assessment of stress evolution in the manufacturing process and upon the electrochemical cycling of SSB electrodes. Such a model is proposed to provide more understanding of the electrochemistry-mechanics couplings that are challenging to evaluate experimentally. The influence of uniaxial and isostatic compression on the ionic and electronic conductivity of SSB cathodes provides a better perspective for optimizing cycling protocols and enhancing battery performance.

Our results highlight the dynamic relationship between pressure, microstructure, and conductivity. Uniaxial compression, while effective in achieving structural compactness with increased conductivity, poses challenges such as AM cracking and reduced battery lifespan due to high stress levels. In contrast, isostatic compression offers a less damaging alternative, resulting in well compacted electrodes with comparable conductivity and significantly reduced stress levels. The ability to maintain good structural uniformity through low stress is critical for improving cycling protocols and preserving the health of the AM particles. Furthermore, we observed dynamic shifts in stress distribution, with AM particles experiencing higher stress levels during expansion and a subsequent transfer of stress to SE particles upon contraction during the discharging and charging phases. This underscores the importance of understanding stress dynamics throughout the battery cycle for optimizing performance and longevity.

Isostatic compression is a more efficient processing route for SSB cathodes, eliminating the need for high-pressure conditions associated with uniaxial methods. Our modeling results agree with the experimental findings previously reported by some us, confronting them with 3D dynamic mechanistic insights. The ability to achieve optimal electrochemical performance at lower pressures is crucial for streamlining production processes of SSBs and reducing their manufacturing costs in their transition to industry. This work emphasizes the importance of controlled stress distribution in enhancing the cycling performance and longevity of SSB cathodes. It also contributes to the ongoing efforts to develop more efficient and reliable solid-state battery technologies, with implications for a wide range of applications.

CRediT authorship contribution statement

Mohammed Alabdali: Writing – original draft, Software, Methodology, Investigation, Formal analysis, Conceptualization. **Franco M. Zanotto:** Writing – review & editing, Methodology, Investigation, Formal analysis. **Mehdi Chouchane:** Writing – review & editing, Conceptualization. **Alain C. Ngandjong:** Writing – review & editing, Methodology, Conceptualization. **Virginie Viallet:** Writing – review & editing. **Vincent Seznec:** Writing – review & editing, Supervision, Funding acquisition. **Ying Shirley Meng:** Writing – review & editing. **Alejandro A. Franco:** Writing – review & editing, Supervision, Resources, Project administration, Methodology, Funding acquisition, Conceptualization.

Declaration of competing interest

The authors declare that they have no known competing financial interests or personal relationships that could have appeared to influence the work reported in this paper.

Supplementary materials

Supplementary material associated with this article can be found, in the online version, at doi:10.1016/j.ensm.2024.103527.

References

[1] J.L. Brédas, J.M. Buriak, F. Caruso, K.S. Choi, B.A. Korgel, M.R. Palacín, K. Persson, E. Reichmanis, F. Schüth, R. Seshadri, M.D. Ward, An electrifying choice for the 2019 chemistry Nobel Prize: Goodenough, Whittingham, and Yoshino, Chem. Mater. 31 (2019) 8577–8581, https://doi.org/10.1021/ACS.CHEMMATER.9B04345/.
[2] European Commission: Renewable energy directive, (n.d.). https://energy.ec.europa.eu/topics/renewable-energy/renewable-energy-directive-targets-and-rules/renewable-energy-directive_en.
[3] K.B. Hatzell, X.C. Chen, C.L. Cobb, N.P. Dasgupta, M.B. Dixit, L.E. Marbella, M. T. McDowell, P.P. Mukherjee, A. Verma, V. Viswanathan, A.S. Westover, W. G. Zeier, Challenges in lithium metal anodes for solid-state batteries, ACS Energy Lett. 5 (2020) 922–934, https://doi.org/10.1021/ACSENERGYLETT.9B02668.
[4] A. Bielefeld, D.A. Weber, R. Rueß, V. Glavas, J. Janek, Influence of lithium ion kinetics, particle morphology and voids on the electrochemical performance of composite cathodes for all-solid-state batteries, J. Electrochem. Soc. 169 (2022) 020539, https://doi.org/10.1149/1945-7111/ac50df.
[5] D.H.S. Tan, A. Banerjee, Z. Chen, Y.S. Meng, From nanoscale interface characterization to sustainable energy storage using all-solid-state batteries, Nat. Nanotechnol. 153 (15) (2020) 170–180, https://doi.org/10.1038/s41565-020-0657-x.
[6] M.B. Dixit, N. Singh, J.P. Horwath, P.D. Shevchenko, M. Jones, E.A. Stach, T. S. Arthur, K.B. Hatzell, In situ investigation of chemomechanical effects in thiophosphate solid electrolytes, Matter 3 (2020) 2138–2159, https://doi.org/10.1016/j.matt.2020.09.018.
[7] Y. Xiao, K. Turcheniuk, A. Narla, A.-Y. Song, X. Ren, A. Magasinski, A. Jain, S. Huang, H. Lee, G. Yushin, Electrolyte melt infiltration for scalable manufacturing of inorganic all-solid-state lithium-ion batteries, Nat. Mater. 20 (2021) 984–990, https://doi.org/10.1038/s41563-021-00943-2.
[8] K.J. Rhodes, R. Meisner, M. Kirkham, N. Dudney, C. Daniel, Situ XRD of thin film tin electrodes for lithium ion batteries, J. Electrochem. Soc. 159 (2012) A294–A299, https://doi.org/10.1149/2.077203jes.
[9] J. Cannarella, C.B. Arnold, Stress evolution and capacity fade in constrained lithium-ion pouch cells, J. Power Sources 245 (2014) 745–751, https://doi.org/10.1016/j.jpowsour.2013.06.165.
[10] J.A. Lewis, F.J.Q. Cortes, Y. Liu, J.C. Miers, A. Verma, B.S. Vishnugopi, J. Tippens, D. Prakash, T.S. Marchese, S.Y. Han, C. Lee, P.P. Shetty, H.-W. Lee, P. Shevchenko, F. De Carlo, C. Saldana, P.P. Mukherjee, M.T. McDowell, Linking void and interphase evolution to electrochemistry in solid-state batteries using operando X-ray tomography, Nat. Mater. 20 (2021) 503–510, https://doi.org/10.1038/s41563-020-00903-2.
[11] D. Bistri, A. Afshar, C.V. Di Leo, Modeling the chemo-mechanical behavior of all-solid-state batteries: a review, Meccanica 56 (2021) 1523–1554, https://doi.org/10.1007/S11012-020-01209-Y.
[12] J.A. Lewis, J. Tippens, F.J.Q. Cortes, M.T. McDowell, Chemo-mechanical challenges in solid-state batteries, Trends Chem. 1 (2019) 845–857, https://doi.org/10.1016/j.trechm.2019.06.013.
[13] B. Koohbor, L. Sang, Ö.Ö. Çapraz, A.A. Gewirth, N.R. Sottos, In situ strain measurement in solid-state Li-Ion battery electrodes, J. Electrochem. Soc. 168 (2021) 010516, https://doi.org/10.1149/1945-7111/abd60b.
[14] T. Shi, Q. Tu, Y. Tian, Y. Xiao, L.J. Miara, O. Kononova, G. Ceder, High active material loading in all-solid-state battery electrode via particle size optimization, Adv. Energy Mater. 10 (2020) 1902881, https://doi.org/10.1002/AENM.201902881.

[15] S.Y. Han, C. Lee, J.A. Lewis, D. Yeh, Y. Liu, H.-W. Lee, M.T. McDowell, Stress evolution during cycling of alloy-anode solid-state batteries, Joule 5 (2021) 2450–2465, https://doi.org/10.1016/j.joule.2021.07.002.
[16] V. Faka, M.T. Agne, M.A. Lange, D. Daisenberger, B. Wankmiller, S. Schwarzmüller, H. Huppertz, O. Maus, B. Helm, T. Böger, J. Hartel, J.M. Gerdes, J.J. Molaison, G. Kieslich, M.R. Hansen, W.G. Zeier, Pressure-Induced dislocations and their influence on ionic transport in Li + -conducting argyrodites, J. Am. Chem. Soc. 146 (2024) 1710–1721, https://doi.org/10.1021/jacs.3c12323.
[17] S.Z. Oener, L.P. Twight, G.A. Lindquist, S.W. Boettcher, Thin cation-exchange layers enable high-current-density bipolar membrane electrolyzers via improved water transport, ACS Energy Lett. 6 (2021) 1–8, https://doi.org/10.1021/acsenergylett.0c02078.
[18] E. Kazyak, R. Garcia-Mendez, W.S. LePage, A. Sharafi, A.L. Davis, A.J. Sanchez, K.-H. Chen, C. Haslam, J. Sakamoto, N.P. Dasgupta, Li penetration in ceramic solid electrolytes: operando microscopy analysis of morphology, propagation, and reversibility, Matter 2 (2020) 1025–1048, https://doi.org/10.1016/j.matt.2020.02.008.
[19] L. Porz, T. Swamy, B.W. Sheldon, D. Rettenwander, T. Frömling, H.L. Thaman, S. Berendts, R. Uecker, W.C. Carter, Y. Chiang, Mechanism of lithium metal penetration through inorganic solid electrolytes, Adv. Energy Mater. 7 (2017), https://doi.org/10.1002/aenm.201701003.
[20] Q. Tu, L. Barroso-Luque, T. Shi, G. Ceder, Electrodeposition and mechanical stability at lithium-solid electrolyte interface during plating in solid-state batteries, Cell Rep. Phys. Sci. 1 (2020) 100106, https://doi.org/10.1016/j.xcrp.2020.100106.
[21] A. Bielefeld, How to develop useful models for solid-state batteries – a plea for simplicity and interdisciplinary cooperation, Batter. Supercaps. 6 (2023), https://doi.org/10.1002/batt.202300180.
[22] A.C. Ngandjong, T. Lombardo, E.N. Primo, M. Chouchane, A. Shodiev, O. Arcelus, A.A. Franco, Investigating electrode calendering and its impact on electrochemical performance by means of a new discrete element method model: towards a digital twin of Li-Ion battery manufacturing, J. Power Sources. 485 (2021) 229320, https://doi.org/10.1016/J.JPOWSOUR.2020.229320.
[23] T. Lombardo, A.C. Ngandjong, A. Belhcen, A.A. Franco, Carbon-binder migration: a three-dimensional drying model for lithium-ion battery electrodes, Energy Storage Mater. 43 (2021) 337–347, https://doi.org/10.1016/J.ENSM.2021.09.015.
[24] T. Lombardo, F. Lambert, R. Russo, F.M. Zanotto, C. Frayret, G. Toussaint, P. Stevens, M. Becuwe, A.A. Franco, Experimentally validated three-dimensional modeling of organic-based sodium-ion battery electrode manufacturing, Batter. Supercaps. (2022) e202200116, https://doi.org/10.1002/BATT.202200116.
[25] J. Xu, A.C. Ngandjong, C. Liu, F.M. Zanotto, O. Arcelus, A. Demortière, A. A. Franco, Lithium ion battery electrode manufacturing model accounting for 3D realistic shapes of active material particles, J. Power Sources 554 (2023) 232294, https://doi.org/10.1016/J.JPOWSOUR.2022.232294.
[26] M. Alabdali, F.M. Zanotto, V. Viallet, V. Seznec, A.A. Franco, Microstructurally resolved modeling of all solid-state batteries: latest progresses, opportunities, and challenges, Curr. Opin. Electrochem. 36 (2022), https://doi.org/10.1016/J.COELEC.2022.101127.
[27] M. Alabdali, F.M. Zanotto, M. Duquesnoy, A.-K. Hatz, D. Ma, J. Auvergniot, V. Viallet, V. Seznec, A.A. Franco, Three-dimensional physical modeling of the wet manufacturing process of solid-state battery electrodes, J. Power Sources. 580 (2023) 233427, https://doi.org/10.1016/j.jpowsour.2023.233427.
[28] Y. Chen, J. Jang, J. Oh, S. Ham, H. Yang, D. Lee, M. Vicencio, J.B. Lee, D.H.S. Tan, M. Chouchane, A. Cronk, M. Song, Y. Yin, J. Qian, Z. Chen, Y.S. Meng, Enabling uniform and accurate control of cycling pressure for all-solid-state batteries, (n.d.) 1–22. 10.26434/chemrxiv-2023-8s8zw.
[29] C. Kloss, C. Goniva, A. Hager, S. Amberger, S. Pirker, Models, algorithms and validation for opensource DEM and CFD-DEM, Prog. Comput. Fluid Dyn. An Int. J. 12 (2012) 140, https://doi.org/10.1504/PCFD.2012.047457.
[30] F.P. McGrogan, T. Swamy, S.R. Bishop, E. Eggleton, L. Porz, X. Chen, Y. Chiang, K. J. Van Vliet, Compliant yet brittle mechanical behavior of Li 2 S–P 2 S 5 lithium-ion-conducting solid electrolyte, Adv. Energy Mater. 7 (2017), https://doi.org/10.1002/aenm.201602011.
[31] L.S. de Vasconcelos, R. Xu, J. Li, K. Zhao, Grid indentation analysis of mechanical properties of composite electrodes in Li-ion batteries, Extrem. Mech. Lett. 9 (2016) 495–502, https://doi.org/10.1016/j.eml.2016.03.002.
[32] H. Pegel, O. von Kessel, P. Heugel, T. Deich, J. Tübke, K.P. Birke, D.U. Sauer, Volume and thickness change of NMC811|SiOx-graphite large-format lithium-ion cells: from pouch cell to active material level, J. Power Sources. 537 (2022), https://doi.org/10.1016/j.jpowsour.2022.231443.
[33] C.D. Quilty, P.J. West, G.P. Wheeler, L.M. Housel, C.J. Kern, K.R. Tallman, L. Ma, S. Ehrlich, C. Jaye, D.A. Fischer, K.J. Takeuchi, D.C. Bock, A.C. Marschilok, E. S. Takeuchi, Elucidating cathode degradation mechanisms in LiNi 0.8 Mn 0.1 Co 0.1 O 2 (NMC811)/graphite cells under fast charge rates using operando synchrotron characterization, J. Electrochem. Soc. 169 (2022) 020545, https://doi.org/10.1149/1945-7111/ac51f5.
[34] GeoDict Simulation Software Release 2023, by Math2Market GmbH, Germany, (n. d.). 10.30423/release.geodict2023.
[35] P. Žguns, B. Yildiz, Strain sensitivity of Li-Ion conductivity in β-Li3PS4 solid electrolyte, PRX Energy 1 (2022) 023003, https://doi.org/10.1103/PRXEnergy.1.023003.
[36] L. Porz, A.J. Klomp, X. Fang, N. Li, C. Yildirim, C. Detlefs, E. Bruder, M. Höfling, W. Rheinheimer, E.A. Patterson, P. Gao, K. Durst, A. Nakamura, K. Albe, H. Simons, J. Rödel, Dislocation-toughened ceramics, Mater. Horizons. 8 (2021) 1528–1537, https://doi.org/10.1039/D0MH02033H.

[37] Y. Zheng, T.J. Slade, L. Hu, X.Y. Tan, Y. Luo, Z.-Z. Luo, J. Xu, Q. Yan, M. G. Kanatzidis, Defect engineering in thermoelectric materials: what have we learned? Chem. Soc. Rev. 50 (2021) 9022–9054, https://doi.org/10.1039/D1CS00347J.

[38] A. Torayev, A. Rucci, P.C.M.M. Magusin, A. Demortière, V. De Andrade, C.P. Grey, C. Merlet, A.A. Franco, Stochasticity of pores interconnectivity in Li–O 2 batteries and its impact on the variations in electrochemical performance, J. Phys. Chem. Lett. 9 (2018) 791–797, https://doi.org/10.1021/acs.jpclett.7b03315.

[39] S. Ohno, T. Bernges, J. Buchheim, M. Duchardt, A.K. Hatz, M.A. Kraft, H. Kwak, A. L. Santhosha, Z. Liu, N. Minafra, F. Tsuji, A. Sakuda, R. Schlem, S. Xiong, Z. Zhang, P. Adelhelm, H. Chen, A. Hayashi, Y.S. Jung, B.V. Lotsch, B. Roling, N.M. Vargas-Barbosa, W.G. Zeier, How certain are the reported ionic conductivities of thiophosphate-based solid electrolytes? An interlaboratory study, ACS Energy Lett. 5 (2020) 910–915, https://doi.org/10.1021/acsenergylett.9b02764.

[40] R. Fantin, E. Trevisanello, R. Ruess, A. Pokle, G. Conforto, F.H. Richter, K. Volz, J. Janek, Synthesis and postprocessing of single-crystalline LiNi 0.8 Co 0.15 Al 0.05 O 2 for solid-state lithium-ion batteries with high capacity and long cycling stability, Chem. Mater. 33 (2021) 2624–2634, https://doi.org/10.1021/acs.chemmater.1c00471.

[41] C. Wang, R. Yu, S. Hwang, J. Liang, X. Li, C. Zhao, Y. Sun, J. Wang, N. Holmes, R. Li, H. Huang, S. Zhao, L. Zhang, S. Lu, D. Su, X. Sun, Single crystal cathodes enabling high-performance all-solid-state lithium-ion batteries, Energy Storage Mater 30 (2020) 98–103, https://doi.org/10.1016/j.ensm.2020.05.007.

[42] C. Doerrer, I. Capone, S. Narayanan, J. Liu, C.R.M. Grovenor, M. Pasta, P.S. Grant, High energy density single-crystal NMC/Li 6 PS 5 Cl cathodes for all-solid-state lithium-metal batteries, ACS Appl. Mater. Interfaces 13 (2021) 37809–37815, https://doi.org/10.1021/acsami.1c07952.